

Supercapacitor Degradation: Understanding Mechanisms of Cycling-Induced Deterioration and Failure of a Pseudocapacitor

Katrina Mazloomian,^[a] Hector J. Lancaster,^[b] Christopher A. Howard,^[b] Paul R. Shearing,^[a, c] and Thomas S. Miller^{*[a, c]}

Owing to a reputation for long lifetimes and excellent cycle stability, degradation in supercapacitors has largely been overlooked. In this work, we demonstrate that significant degradation in some commercial supercapacitors can in fact occur early in their life, leading to a rapid loss in capacitance, especially when utilized in full voltage range, high charge-discharge frequency applications. By using a commercial 300 F lithium-ion pseudocapacitor rated for 100,000 charge/discharge cycles as an example system, it is shown that a ~96% loss in capacitance over the first ~2000 cycles is caused by significant structural and chemical change in the cathode active material (LiMn_2O_4 , LMO). Multi-scale in-situ and ex-situ characterization, using a combination of X-ray computed tomography, Raman spectroscopy and X-ray photoelectron spectroscopy, shows that while

minimal material loss (~5.5%), attributed to the dissolution of Mn^{2+} , is observed, the primary mode of degradation is due to manganese charge disproportionation ($\text{Mn}^{3+} \rightarrow \text{Mn}^{4+} + \text{Mn}^{2+}$) and its physical consequences (i.e. microstrain formation, particle fragmentation, loss of conductivity etc.). In contrast to prior understanding of LMO material degradation in battery systems, negligible contributions from cubic-to-tetragonal phase transitions are observed. Hence, as supercapacitors are becoming more widely utilized in real-world applications, this work demonstrates that it is vital to understand the mechanisms by which this family of devices change during their lifetimes, not just for lithium-ion pseudocapacitors, but for a wide range of commercial chemistries.

Introduction

Supercapacitors have generated widespread interest in the field of energy storage because of their unique characteristics of high-power density, good reversibility and rapid rate of charge/discharge.^[1] These characteristics allow them to fill a critical gap in the gamut of electrochemical energy storage systems between batteries and capacitors for use in a variety of industries including consumer electronics,^[2] automobiles,^[3] robotics,^[4] military^[5] and medical applications.^[6,7]

It is widely accepted that 'supercapacitors have long cycle lifetimes',^[8,9] largely based on the behavior of some pure electrochemical double layer capacitors (EDLCs), which are often advertised to offer up to 500,000 or even 1,000,000 duty cycles.^[10,11] However, this performance should be considered in the context that a supercapacitor in, for example, a regenerative braking system, may experience hundreds, if not thousands of charge/discharge events in a day.^[12,13] Hence their cycle life may be significantly longer than other technologies, but their calendar life could be more similar. Additionally, quoted lifetimes are typically calculated under highly favorable conditions, both electrochemically and environmentally, using very slow charge/discharge rates over reduced voltage ranges and under controlled temperature and humidity conditions. This is far from the fast charge/discharge, full voltage range conditions that many supercapacitors will experience in their daily life in operating commercial devices. A reputation for a high cycling stability has, however, meant that the mechanisms by which supercapacitors degrade and fail have unfortunately been studied far less than those for batteries, hindering the development of high-performance next-generation systems.

The issue of supercapacitor degradation is likely even more significant for pseudocapacitors, a subset of supercapacitor devices that are distinguished from EDLCs as they utilise fast and reversible redox reactions at the surface of the electrodes to store charge chemically, as opposed to electrostatically separating charges.^[14] These also include lithium-ion capacitors in which the main charge storage reactions occurring at the

[a] K. Mazloomian, Prof. P. R. Shearing, Dr. T. S. Miller
Electrochemical Innovation Lab, Department of Chemical Engineering,
University College London, London, WC1E 7JE, U.K.
E-mail: t.miller@ucl.ac.uk
Homepage: <http://www.ucl.ac.uk/electrochemical-innovation-lab>
<http://www.ucl.ac.uk/chemical-engineering/people/dr-thomas-miller>

[b] H. J. Lancaster, Prof. C. A. Howard
Department of Physics & Astronomy, University College London, London
WC1E 6BT, U.K.

[c] Prof. P. R. Shearing, Dr. T. S. Miller
The Faraday Institution, Quad One, Harwell Science and Innovation
Campus, Didcot OX11 0RA, U.K.

 Supporting information for this article is available on the WWW under
<https://doi.org/10.1002/batt.202300214>

 © 2023 The Authors. Batteries & Supercaps published by Wiley-VCH GmbH.
This is an open access article under the terms of the Creative Commons
Attribution License, which permits use, distribution and reproduction in any
medium, provided the original work is properly cited.

electrodes specifically involve a lithium ion as the main charge carrier traveling between the anode and cathode.

The ability of pseudocapacitors to rapidly charge and discharge is thus possible through the use of high surface area materials, resulting in a charge storage mechanism that is not hindered by slow diffusion into the bulk, mechanically distinguishing them from batteries.^[15] However, as a consequence of utilizing faradaic reactions, based on a wide range of chemistries, pseudocapacitive materials are known to suffer from chemical side reactions, similar to those that cause cell deterioration in batteries.

To date, supercapacitor degradation has largely been studied using methods based on impedance spectroscopy and commonly modeled mathematically in numerous RC (resistor-capacitor) circuit configurations.^[16–18] For example, the study by Bohlen et al. developed calendar aging models for supercapacitors under the assumption that the capacitance decreased linearly with time at a constant voltage and temperature.^[18] However, studies such as this do not account for variables such as dynamic voltage fluctuations and other deviations from ideality that inevitably occur in realistic use. More importantly, they do not actually explain why the supercapacitor is degrading; whether through structural or chemical changes, mechanical stress, poor device engineering, or other mechanisms. Therefore, directions to improve the stability and cycling performance of these systems are lacking.

In contrast, the study of degradation in batteries has become a major area of research with numerous tools having been optimized to assess their structural and material changes *in situ*. In particular, X-ray computed tomography (CT) has been used to demonstrate key failure modes of Li-ion batteries, such as in instances of thermal runaway, to reveal more subtle mechanisms of degradation through the study of statistically significant 3D reconstructions of the microstructure.^[19–22] However, despite proving to be extremely useful in battery research, X-ray CT has yet to be extended to the understanding of supercapacitor degradation and failure. The few studies linked to supercapacitors simply focus on materials development and use X-ray CT for the *ex situ* structural characterization of electrode materials.^[23,24]

In this work, we utilize a multiscale characterization approach combining electrochemical analysis with X-ray CT and complementary spectroscopic, microscopic and diffraction analysis to reveal the modes of degradation in a commercial supercapacitor over its full charge/discharge cycle lifetime. Importantly, while the pseudocapacitor system studied was rated for long lifetimes of up to 100,000 cycles, it was in fact found to suffer from extreme degradation under full voltage range cycling, linked to severe material change at the cathode; the mechanistic understanding developed also has implications for the study of high-rate batteries. These findings therefore provide new insights into the aging processes of pseudocapacitors and highlight how essential it is to develop an in-depth knowledge of supercapacitor degradation, before these devices become even more widely utilized in commercial applications.

Results and Discussion

Electrochemical performance

The capacitance (F) of the first 100,000 charge/discharge cycles of a commercial 300 F pseudocapacitor (Maxwell, Model Number PCAP0300 P230 S07)^[25] is shown in Figure 1(a). Tests were performed within the manufacturer's rated voltage range of 0–2.3 V at a constant current of 5 A (rated maximum current: 53 A).

Supercapacitors are very commonly advertised as being able to maintain capacity and remain stable throughout their long lifetimes of up to hundreds of thousands of cycles,^[10,11] yet here, the full-life cycling data shows a swift and drastic decrease in the overall capacitance from ~328 F in the first cycle to 2.5 F for the 100,000th. This behavior was consistent across several repeats with different cells as shown in Figure S1 (Supporting Information). The inset in Figure 1(a) focuses on the first 3000 cycles where most of the dynamic activity is observed, showing that the vast majority of capacity loss occurs before ~2000 cycles where the capacity measured was only 11.3 F. Discharge capacitance values were calculated for each cycle and follow the same trend as presented in Figure S2 along with charge and discharge energy values. Together, this data indicates that full voltage range cycling, even at relatively low current densities, significantly accelerates degradation for this cell chemistry.

Data from select charge/discharge cycles is presented in Figure 1(b). From these voltage-time plots, it can be observed that a significant increase in the degree of self-discharge is shown to occur during the 30 second rest period between the charge and discharge steps as cycling proceeds. This reflects a weakened energy retention that progresses upon aging. A small degree of voltage leak, in line with that occurring during the first 200 cycles, is expected for any supercapacitor as there is often some current that passes between electrodes while at rest due to Gibbs free energy-driven charge redistributions. However, by 500 cycles there is a significant increase in the voltage lost as highlighted in the plot of the voltage drop vs. cycle number in Figure 1(c). An increase of self-discharge from 0.22 V in the first cycle to 0.47 V for the 500th cycle is observed with losses continuing up to ~4000 cycles, where the self-discharge peaks at ~1 V before it goes on to stabilize at ~0.9 V for the remainder of the cell lifetime. The inset in Figure 1(c) highlights the activity from 1 to 4000 cycles. Voltage losses have a direct impact on the energy available and power of the supercapacitor as both these values are proportional to the square of the voltage. A loss this drastic can render the performance of the supercapacitor unreliable and ineffective.

Another changing feature of the data in Figure 1(b) is the profile of the charge and discharge curves as cycling proceeds. In particular, at the beginning of life, the voltage changes pseudo-linearly against time during both charge and discharge. However, in as few as 100 cycles, evidence of degradation can be seen in the voltage trace; at ~0.5 V, the decrease in voltage during discharge is no longer linear and instead exhibits a steep drop. This becomes exaggerated and shifts to higher potentials

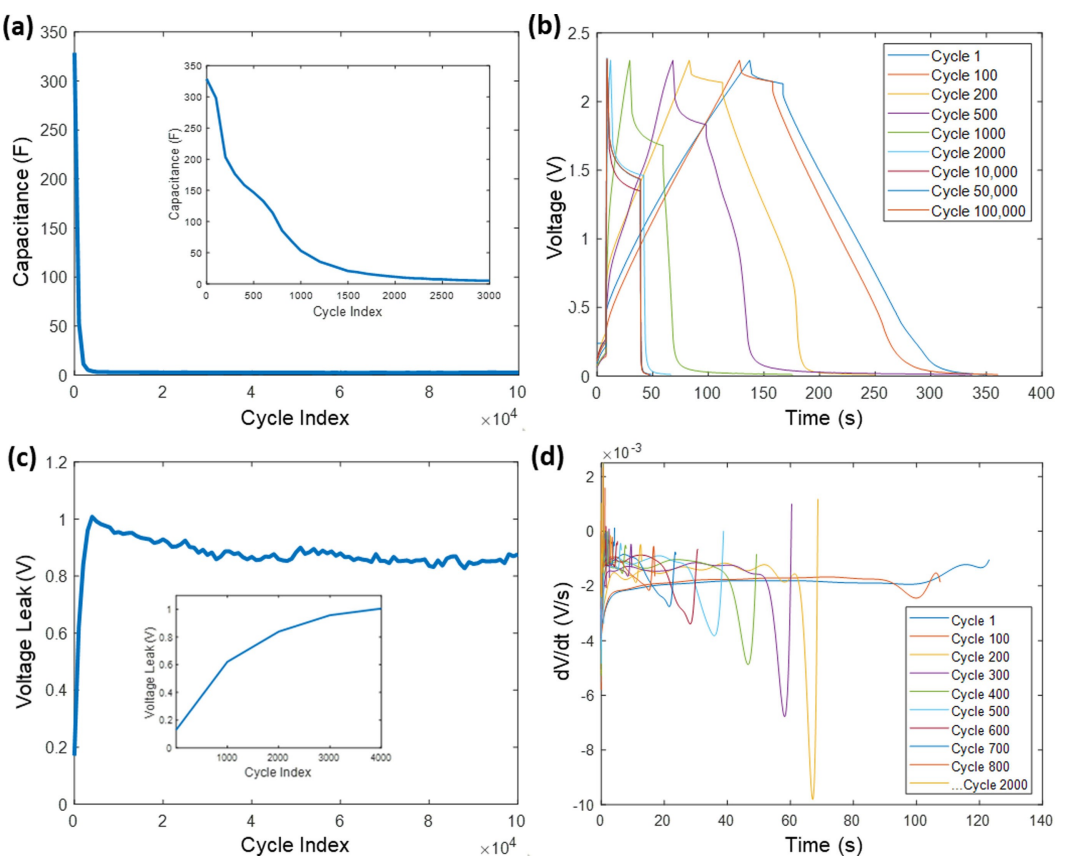


Figure 1. Electrochemical cycling. a) Charge capacitance (F) plotted against the respective cycle number over 100,000 charge/discharge cycles with the inset highlighting cycles 1–3000. b) Charge/discharge curves of the voltage (V) over time (s) for various cycles. c) The voltage leak (V) during the 30 second rest period between charge and discharge steps for each of the 100,000 cycles. d) The gradients of the discharge curves for various cycles.

as cycling continues, as emphasized in Figure 1(d) where dV/dt vs discharge cycle time is plotted to highlight inflection points. As the valleys correspond to inflection points of the curves in Figure 1(b), their shallowing after ~ 200 cycles confirms increasing voltage drop-off values and reflects a progressing degradation. Comparable drop-off behavior is exhibited by similar lab-built cells in the literature.^[26] As the cells have been cycled within the recommended voltage limits and do not show any signs of puncturing that would cause exposure to air, solvent degradation is tentatively excluded as a cause for this degradation. There is also no indication of short circuit leakage currents. Hence, self-discharge via parasitic faradaic reactions is the most likely cause,^[27] the origin of which depends on the cell chemistry and is further explored below.

Characterizing cell chemistry and electrode composition

Deconstruction of representative non-cycled cells showed that the commercial supercapacitor being studied utilizes a Li-ion chemistry with asymmetric electrodes – i.e., it is a hybrid lithium-ion capacitor. As discussed below, the active cathode material is lithium manganese (III) manganese (IV) oxide (LiMn_2O_4 , LMO), while the anode consists primarily of micro-

crystalline disordered carbon, similar to carbon black or active carbon.

The indexed X-ray diffraction (XRD) pattern of the cathode material scraped from the current collector shows all characteristic features of LMO (Figure S3), with no other observable crystalline material. Scanning electron microscopy (SEM) images show that the active particles are embedded in a graphitic carbon and a polymeric binder domain (Figure 4b and 4c). SEM (Figure S4), X-ray photoelectron spectroscopy (XPS) (Figure S5) and Raman analysis (Figure S6) of the anode show characteristic features which are consistent with those expected for a microcrystalline disordered carbon, as opposed to graphite which is typically used in lithium-ion battery anodes. Both electrodes use aluminum foil current collectors and are coated on both sides. The electrolyte used appears to be an organic solution of tetraethylammonium tetrafluoroborate (TEABF₄) dissolved in acetonitrile as determined by the Raman and XPS data of the salt and the mass spectroscopy data of the solvent (Figure S7).

Modes of degradation

Although the cell electrode/electrolyte materials themselves are common sources of degradation in electrochemical storage

devices, mechanical, electrical and cell engineering faults are also typical sources of failure that should be investigated.

To show the impact of the cycling at the full cell level, *in situ* X-ray CT images were obtained of pristine and degraded cells. The reconstructed tomograms show the most X-ray attenuating materials as white and the least attenuating as black. Figure 2 presents side angle (Figure 2a) and top-down (Figure 2b) cross-sections of a cell before it was cycled, showing that the electrode coil consists of double-side coated LMO (white) and carbon (dark grey) electrodes on aluminum current collectors (light grey) with a polymer separator in between. The separator is difficult to distinguish as it exhibits low attenuation of the X-ray beam.

There is a significant difference in thickness between the cathode ($\sim 35 \mu\text{m}$) and anode ($\sim 115 \mu\text{m}$), as highlighted in Figure 2(c), which suggests that the energy density of the LMO material is larger than that of the carbon. The current collectors are connected to the terminals via two pins situated halfway through the electrode coil which has been wrapped around a paper support structure. Importantly, significant manufacturing defects that could contribute to rapid degradation could not be detected in the cell, or any of the other cells tested, prior to cycling.

These images show that the pseudocapacitor is somewhat architecturally similar to typical cylindrical cell lithium-ion batteries (e.g., LG 18650 NMC cells).^[21] There are important differences, however, that distinguish the two systems from one another. While both typically consist of two spiral-wound electrodes wrapped in a coil and housed in a steel casing, the supercapacitor operates at higher current densities and thus must be engineered to account for instances of rapid gassing with an extra gap between the coil and casing wall, as shown in

Figure 2(b). This acts as a necessary safeguard against potential gas build-up during degradation. The low boiling point of acetonitrile (81.6°C), compared to other electrolyte solvents used in energy storage devices, may exacerbate gas generation during cycling, increasing the risk of cell expansion or even rupture. Typical Li-ion battery systems, on the other hand, tend to use alkyl carbonate-based solvents with higher boiling points for their electrolytes, meaning gas volumes tend to be lower and develop more slowly.^[28]

A further difference is that this supercapacitor has tabs positioned in the center of the coil, 90° away from each other that extend through the entire length of the cell, resulting in protruding pins that come out of the same terminal end. Cylindrical batteries, in contrast, generally have shorter tabs that are positioned 180° away from each other, and are connected to opposing terminal ends.^[29] Tab position and design can significantly impact the performance and safety of a cell as it can impact the chance of short circuits.^[29] In addition, the temperature around the tab is often much higher during cycling than other areas due to the current concentration around the metal fixtures.^[29] As a result, the same macroscopic structural damage that batteries experience upon cycling may not be consistent with supercapacitor failure.

Moreover, it is common in current lithium-ion batteries for the anode and cathode to be mounted on different current collectors; aluminum for the cathode and copper for the anode. However, as denoted in Figure 2(c), this supercapacitor has both electrodes mounted on aluminum, a choice that can help reduce costs while still maintaining a high conductivity. Aluminum, however, is more likely to form a passivation layer on its surface which may be the cause of the flaking and adhesion issues observed in the anode after cycling.^[30] The

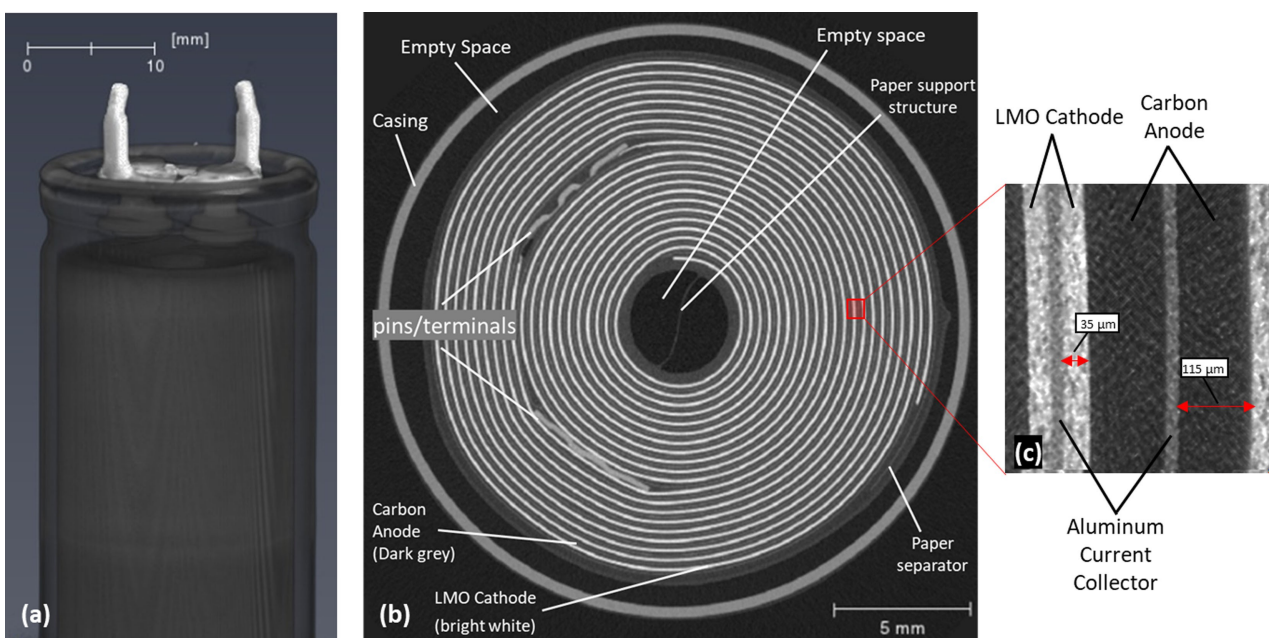


Figure 2. X-ray CT of a Li-ion pseudocapacitor. Full cell images of the pseudocapacitor showing a) the side view and b) top-down cross-sectional view of the full pristine cell. c) The top-down view shows the alternating cathode (bright electrode) and anode (dark electrode) electrode coil structure with the inset highlighting the difference in thickness of the two electrodes.

architectural differences between this supercapacitor and a typical Li-ion battery may lead to dramatic differences in how each device will ultimately fail, despite the fact that they could operate with similar active materials in their electrodes.

Equivalent X-ray CT images were subsequently collected at the same macroscale resolution after 50,000 and 100,000 charge/discharge cycles as shown in Figure 3. Studies such as those by Finegan et al.^[21] have shown that the first indications of catastrophic failure of Li-ion battery cells are gas-induced electrode delamination, structural deformation, electrode layer collapse and material cracking; electrode deformation, contortions and damage have also been observed in cells cycled using manufacturer recommended conditions.^[31,32] However, no obvious signs of any of these phenomena were found from the CT images of the pseudocapacitor at this scale. Measurements of the coil circumference and the shell diameter remained constant, eliminating large-scale electrode swelling or distortions as a major contributor to the degradation.^[33,34] This highlights that even for Li-ion capacitors, mechanisms of degradation can be distinct from equivalent batteries, due to their differing composition and engineering.

Analysis of the individual cell components suggested that the cathode is likely the main source of the most significant

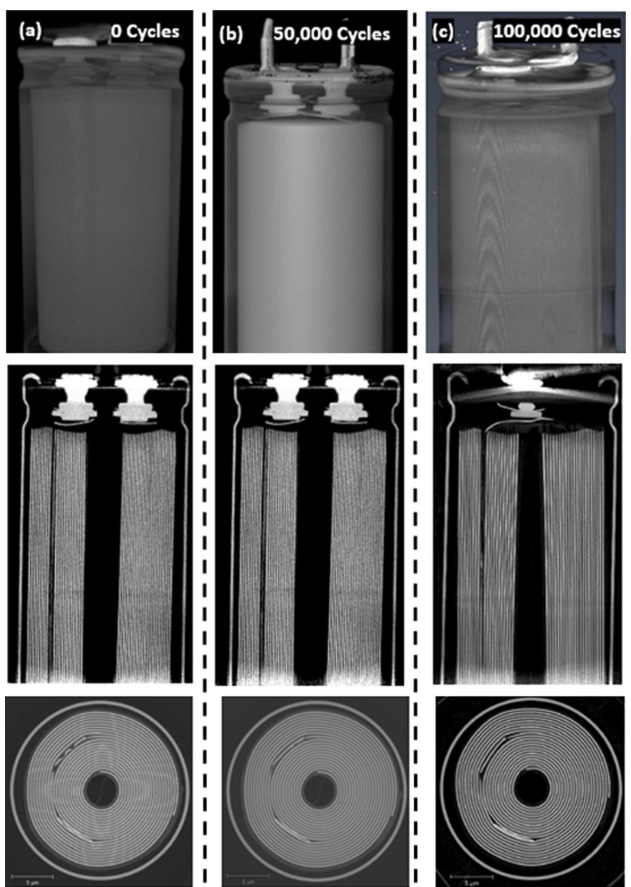


Figure 3. X-ray CT of pristine and degraded lithium-ion capacitors. Full cell images showing (from top to bottom) the 3D cell, characteristic slice in the XY direction and characteristic slice in the XZ direction for the pseudocapacitor after a) 0 cycles, b) 50,000 cycles and c) 100,000 cycles.

mechanisms of degradation. Raman mapping of the anode surface showed minimal change in the D to G peak area ratio (A_D/A_G) of the primarily carbon electrode, which is a metric used to indicate the degree of disorder in graphitic materials, with smaller values corresponding to lower levels of disorder.^[35,36] The histograms comparing the A_D/A_G ratio of the pristine and degraded anode presented in Figure S8 show a minimal increase upon cycling from a mean value of 1.39 ± 0.47 (standard deviation) to 1.44 ± 0.24 , suggesting no significant change over 100,000 charge/discharge cycles. SEM images of the pristine and degraded anode (Figure S4) further show that the graphitic platelets maintained their particle shape and thus exhibit no obvious signs of failure.

Electrolyte decomposition in supercapacitors has also been identified as a possible source of system degradation in many cases,^[37] however, restricting electrochemical testing to within the electrolyte's rated voltage limits should eliminate this as a key driving force.

Powder XRD patterns of the cathode were collected by removing the electrode material from a pristine pseudocapacitor cell (PCAP0300 P230 S07) and reveal that the LMO material has a spinel crystal structure consisting of a cubic close-packed oxygen framework (Figure 4a). In this structure, the Li^+ ions occupy the tetrahedral sites and Mn(III) and Mn(IV) occupy the octahedral sites in a 1:1 ratio (ICSD Collection Code: 89985). The spinel's open framework, in combination with easy recovery of Mn–O chemical bonds to initial electronic states after Li occupation, is ideal for easy charge storage via a two-stage Li-ion insertion/de-insertion that can provide a high power density and good reversibility for supercapacitors. No additional impurity peaks were observed, suggesting the other cathode components consist of amorphous binders and conductive carbon additives such as activated carbon or carbon black that would typically be used to aid electrode conductivity for materials with wide band gaps, i.e., LMO (band gap: 1.16 eV).^[38] This is further supported by the full range Raman spectrum that shows the cathode to have manganese oxide signatures along with typical disordered carbon peaks that emerge in the 1300–1600 cm^{-1} region (Figure S9).

While there are many advantages of using LiMn_2O_4 , it has been shown in batteries to suffer from weak cycling performance and rapid capacity fade due to material degradation.^[39] XRD patterns of the LMO cathode materials in this study were collected after being subjected to 100,000 charge/discharge cycles (Figure 4a). These show a ~40% intensity drop after cycling that points to a possible loss of periodicity from material breakdown. Moreover, peak broadening of ~25% observed in the degraded sample may suggest the emergence of either strain, variations/defects or the formation of smaller crystallite domains. Other studies have observed similar peak broadening of LMO when used in the context of a battery and have correlated this with the device's capacity loss as a result of emerging disorder in the spinel structure.^[40]

Morphological consistency is however likely maintained as the peak intensities between the pristine and degraded samples remain proportional to one another.^[41] This is further confirmed in the SEM images in Figure 4 in which the pristine (Figure 4b)

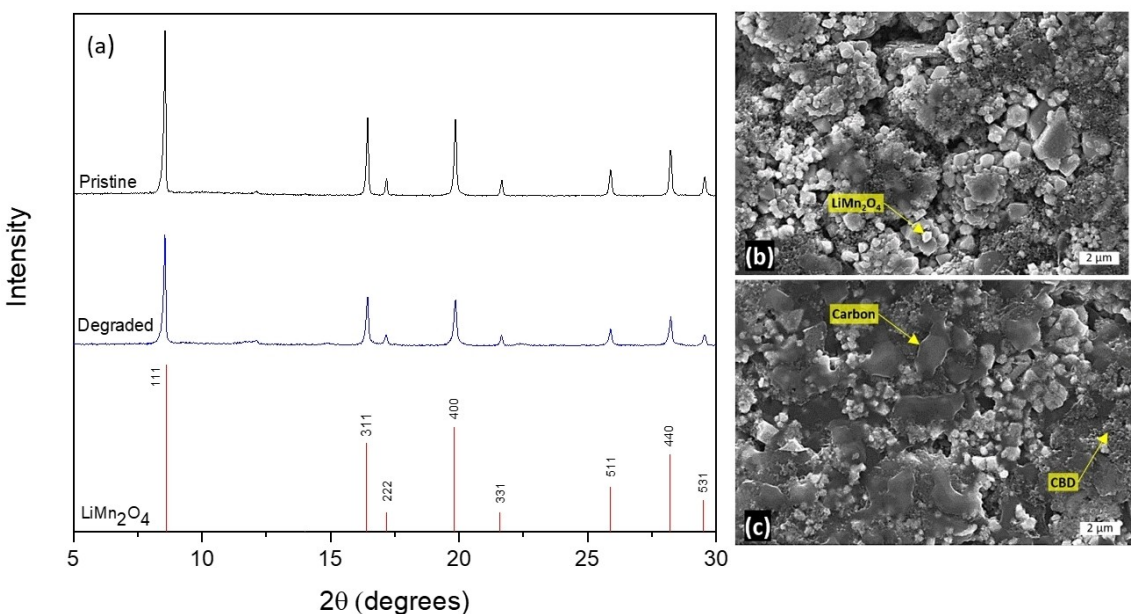
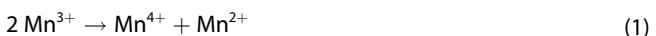


Figure 4. Characterization of the LMO cathode. a) XRD pattern of LiMn₂O₄ (ICSD Collection Code: 89985) (red) as compared to the patterns of the supercapacitor cathode before (black) and after (blue) cycling. Data obtained using a Mo K α 1 X-ray radiation source. Scanning electron microscopy images of the b) pristine and c) degraded LMO cathode.

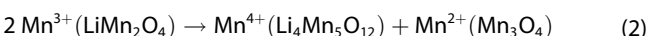
and degraded (Figure 4c) cathode show a combination of defined LiMn₂O₄ particles, conductive carbon platelets and webbed carbon binder domains (CBD). The largest particles exhibit a polyhedral crystalline shape not widely observed in the smaller fragments. Zhu et al. explain that the LMO's wide particle size distribution and polyhedral structure are key to causing structural instability and capacity fading issues as the material exists in two different states during cycling in which surface particles are "Li-rich" and embedded materials are "Li-poor".^[42] The nonuniformity of these two different states adds stress and structural disfigurement/instability leading to poor performance.

Once degraded, areas of the electrode are noticeably void of active LMO particles suggesting surface detachment/dissolution and a possible breakdown and diffusive spread of carbon fragments. As no major structural damage was observed from the macroscale CT images, these particle-scale changes, that have more to do with the chemistry and electronic behavior of the material, must be understood to uncover the reasons for early cell failure.

Many studies have proposed a combination of mechanisms to explain the degradation of LMO materials in batteries, which is viewed as being governed by two major processes. First, disproportionation of Mn³⁺ (i.e., the Hunter mechanism).^[43]



Recent studies have linked the disproportionation of Mn³⁺ from LiMn₂O₄ to the somewhat irreversible formation of Li₄Mn₅O₁₂ (Mn⁴⁺) and Mn₃O₄ (Mn²⁺) as stated more explicitly in Eq. (2).^[44,45]



Mn²⁺ in the form of Mn₃O₄ is soluble in most electrolytes, including acetonitrile,^[46] meaning up to 25 % of the Mn present could theoretically dissolve.^[43] This provides a possible explanation for the patches of void LMO areas seen in the SEM images (Figure 4b and 4c) that point to issues with surface detachment/dissolution. Additionally, the onset of this reaction has also been thought to result in a loss of crystallinity during cycling^[47] and uneven Li diffusion.^[44]

The second process involves the formation of tetragonal Li₂Mn₂O₄ on the surface of LiMn₂O₄ due to associated Jahn-Teller distortions during periods of deep discharge.^[48] This can cause inhomogeneous and irreversible cubic-to-tetragonal phase transformations, cation mixing between lithium and manganese, volume expansions/structural fatigue leading to crack propagation and a loss of particle-to-particle contact.^[48,49]

These mechanisms have been determined in the context of battery degradation, where the current drawn is relatively low. However, pseudocapacitor cycling requires much higher current densities and therefore may drive different failure mechanisms which have yet to be verified experimentally. Hence, to assess the source of this degradation at the individual particle level in a pseudocapacitor, higher resolution X-ray CT images were collected from within the cathode structure and presented in Figure 5.

3D models and corresponding cross-sectional slices of the XY plane (see methods) are presented in Figure 5(c and d) for the pristine electrode and Figure 5(g and h) for the degraded. The models show sufficient likeness to the original reconstructed X-ray images for reliable statistical analysis to take place. Values reported are an average of three segmentations,

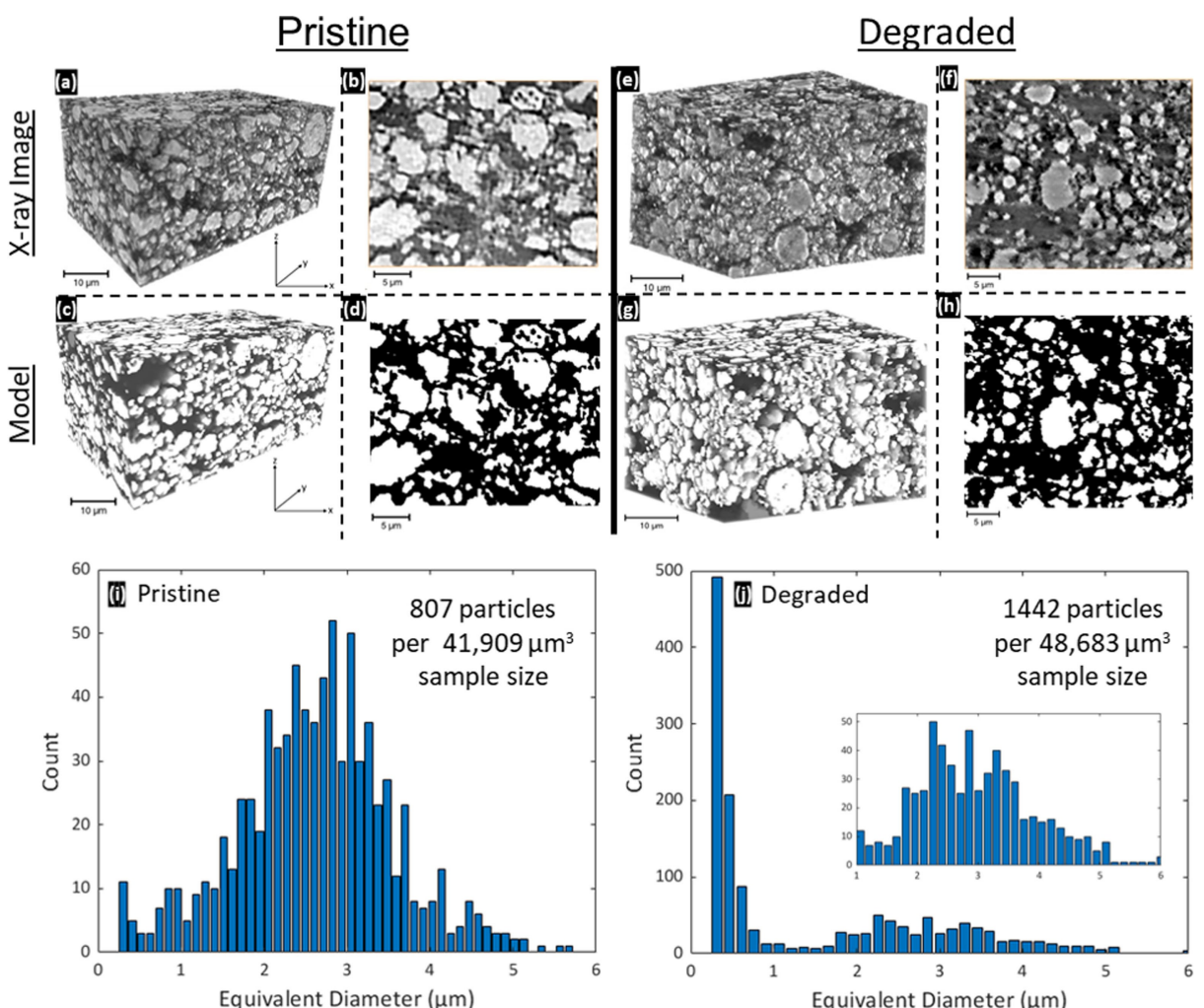


Figure 5. High resolution X-ray CT of LMO cathode materials a) 3D volume rendering of the pristine LMO electrode with b) a characteristic cross-sectional slice in the XY orientation. c) and d) are the same images of the electrode from the 3D model built using a moderate threshold in the Avizo 3D visualization software and are shown to be a good match. e–h) present the corresponding images for the degraded electrode. i) and j) present graphs of the particle size distribution for the pristine and degraded cathode, respectively, using a moderate threshold model.

however the complete set of results for each segmentation can be found in Table S1 in the Supporting Information.

It has been traditionally accepted that transition metal dissolution is the root cause of capacity fading, however, the data shows clear visual evidence of this only occurring to a moderate degree here. A decrease of only 5.5% in the average volume of the cathode electrode occupied by LMO particles is observed from X-ray CT; this can be explained as a consequence of Mn^{2+} material dissolution via the Hunter mechanism. XPS analysis was performed on the anode of both pristine and degraded supercapacitor cells and did confirm a small increase in the Mn concentration at the anode surface from roughly 0.3 at% to 6.9 at% after cycling (Figure S5). The interaction of Mn ions with the anode has been shown to be directly associated with capacity fading and self-discharge issues in batteries,^[50] and this appears to occur to some degree in the supercapacitor being studied here. In particular, the reaction of Mn species with Li ions at the anode is expected to be a primary source of the self-discharge observed in Figure 1 during

early cycles, although (redox active) cathode material deactivation will also cause the cell storage mechanism to tend towards double layer capacitance, where self-discharge is a known issue. Nonetheless, the extent of material loss measured from the cathode, and gain observed at the anode, is largely insubstantial in comparison to the drastically low capacity retention of ~4% after only a fraction of the cell's expected lifetime (2000 cycles out of 100,000). This suggests material dissolution is a minor, secondary, driver of degradation here.

This discrepancy with the traditional interpretation of the Hunter mechanism may be understood by considering the different kinetics of batteries vs supercapacitors. The dissolved Mn concentration has previously been quantified in batteries via analysis of the anode to show LMO material migration through the cell.^[44] In supercapacitors however, faster cycles leaves less time for the Mn^{2+} species formed on the cathode surface to dissolve and diffuse before the polarity is switched and can thus reduce amounts of detectable manganese on the anode.

More fundamentally, Hunter's original experiment looked at LMO that was first stirred and then decanted, significantly enhancing dissolution due to system agitation. A distinction must therefore be made between Mn^{3+} disproportionation and Mn^{2+} dissolution, the former being the degradation mechanism that results when the Mn oxidation state in LMO drops below +3.5, and the latter being a resultant kinetics/mass-transport dependent phenomenon. This conclusion is further supported by Raman mapping, which showed that little Mn could be detected on the anode surface across a $100 \times 100 \mu\text{m}$ area (Figure S6), which may indicate the Mn observed in the XPS experiments (Figure S5) was limited to the interface, due to the high surface sensitivity of XPS. This understanding of the degradation coincides with reports from the literature that have experienced a similar disconnect between a modest degree of material loss and contrastingly sizable capacity fade.^[40,51]

Interestingly, the X-ray CT data shows a significant non-uniformity within the cathode particles with a large LMO particle size distribution that ranges from 0.19 to $6.13 \mu\text{m}$. This indicates that there are large agglomerates that may unfavorably cause heightened resistance to ion surface accessibility that can hinder charge storage in high power density devices. In addition, the average pre-cycling LMO particle diameter of $2.19 \mu\text{m}$ is surprisingly large as nanoparticles with larger surface area-to-volume ratios are typically preferred for supercapacitor electrodes.²⁶ This value decreases by 37% to $1.37 \mu\text{m}$ after cycling pointing to possible microstrains that can cause particle fragmentation or a loss of agglomerate material.

Particle size distributions for all three segmentations (see methods) can be found in Figure S10(a–c) for the pristine sample and Figure S10(d–f) for the degraded sample. The normal distribution of particle sizes observed in the pristine electrode, with a mean of $2.22 \mu\text{m}$, skews considerably towards the nanometer size after cycling to a mean of $1.29 \mu\text{m}$ as presented in Figure 5(i and j) for the moderate segmentation threshold. An emergence of smaller particles again points to microstructure formation and particle fracture. These results were consistent for all three thresholds of segmentation.

Furthermore, Figure 5 shows that 807 particles were detected within a representative volume of $41,909 \mu\text{m}^3$ for the image renderings of the pristine sample and 1442 particles in a volume of $48,683 \mu\text{m}^3$ for the degraded. This means the particle density increased from an average of ~ 20 to ~ 30 particles per $1000 \mu\text{m}^3$. Additional statistics showed a decrease of $\sim 74\%$ in average 3D area per particle, $\sim 35\%$ in average 3D volume per particle, and 22% in cell tortuosity through the x-direction, all of which suggest that there is a large influence from microcrack

formation, which creates smaller particles with a larger overall surface area, contributing to the structural changes within the electrode material.

Mechanistic understanding of LMO degradation

To probe the degradation mechanisms further, Raman spectroscopy was used. Figure 6 presents three representative point spectra for the pristine (spectra 1–3) and degraded (spectra 7–9) cathode samples after being cycled over the full voltage range (FVR) of 0 – 2.3 V for 100,000 cycles. Both datasets were obtained with the electrode in the discharged state. Peak positions of the most notable features of the pristine cathode are given in Table 1 which specifies the Raman active modes responsible for each peak, as proposed by the works of Julien et al., further supporting the assignment of the cathode material as LiMn_2O_4 .^[52–54] The presence of a shoulder at $\sim 650 \text{ cm}^{-1}$ (peak 6) in almost all spectra is of particular interest. In isolation, this peak is characteristic of Mn_3O_4 , however, alongside the other LMO features, it could also be indicative of $\text{Li}_4\text{Mn}_5\text{O}_{12}$. Both species are degradation products of LMO that have previously been identified by Tang et al.^[45] Eq. (2). Therefore, the peak at $\sim 650 \text{ cm}^{-1}$ is likely a convolution of the Raman signal of both degradation species.

Upon cycling, the most dominant trend observed is the significant growth of this $\sim 650 \text{ cm}^{-1}$ peak across the electrode surface. By comparing Raman maps consisting of 676 points over a $50 \times 50 \mu\text{m}$ area before and after cycling, the accumulation of the degradation species can be effectively studied. The heat maps in Figure 6 show the peak intensity ratio of the $\sim 650 \text{ cm}^{-1}$ mode (peak 6) to the $\sim 560 \text{ cm}^{-1}$ $\text{Li}_x\text{Mn}_2\text{O}_4$ mode (peak 4) for the pristine and FVR-degraded electrodes. The intensity of the $\sim 650 \text{ cm}^{-1}$ mode is seen to overtake as the dominant peak in some instances as highlighted in spectra 8 and 9. At these points, additional Mn_3O_4 characteristic modes at ~ 300 – 310 and 350 – 360 cm^{-1} also emerge, evidencing that unsolvated Mn_3O_4 has developed on the electrode surface as a degradation product rather than $\text{Li}_4\text{Mn}_5\text{O}_{12}$.^[53,54] From the maps, it can be seen that there is large variability on the electrode surface with hotspots of $>30 \mu\text{m}^2$ having developed during full voltage range cycling. This heterogeneity is likely a result of uneven reinsertion of Li-ions upon charge and discharge cycles, creating localized areas of strain that trigger Mn^{3+} disproportionation. This technique allows us to fingerprint localized surface degradation by pointing out areas of particularly high concen-

Table 1. Raman peak positions specifying the active modes that correspond to the distinguishing features of the Raman spectra for the pristine LMO cathode sample.

Peak number	Position [cm^{-1}]	Standard deviation [cm^{-1}]	Attributed species	Proposed Raman mode
1	340	± 4	$\text{Li}_x\text{Mn}_2\text{O}_4$	O–Mn–O bending
2	392	± 4	$\text{Li}_x\text{Mn}_2\text{O}_4$	Li–O bending
3	453	± 5	$\text{Li}_x\text{Mn}_2\text{O}_4$	Mn–O/Li–O stretching
4	564	± 2	$\text{Li}_x\text{Mn}_2\text{O}_4$	Mn–O stretching
5	625	± 5	$\text{Li}_x\text{Mn}_2\text{O}_4$	Mn–O stretching
6	653	± 7	$\text{Mn}_3\text{O}_4/\text{Li}_4\text{Mn}_5\text{O}_{12}$	Mn–O stretching

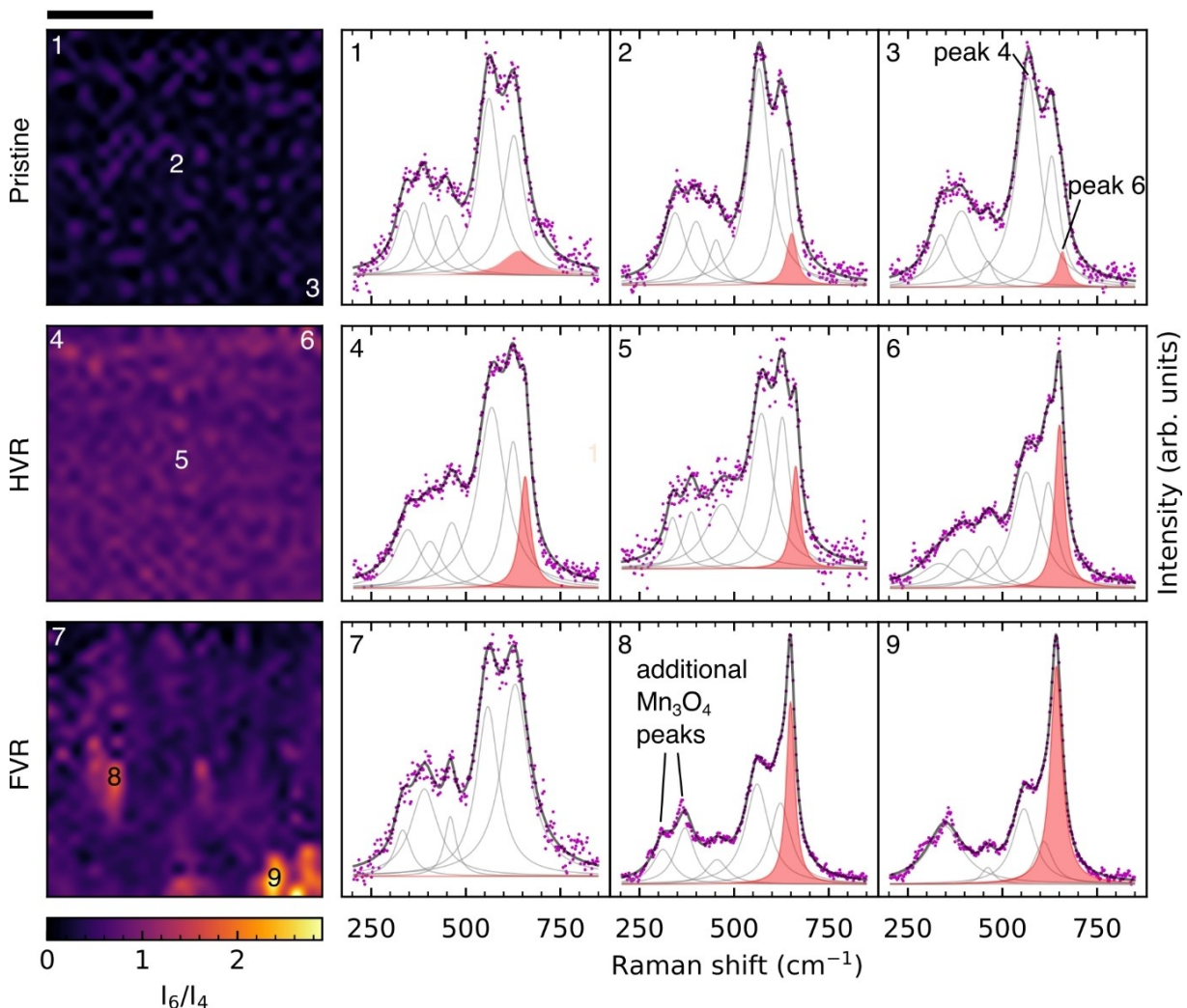


Figure 6. Raman mapping of the LiMn₂O₄ cathode in the range of 200–1900 cm⁻¹ for the (top to bottom) pristine, high voltage range (HVR) degraded and full voltage range (FVR) degraded electrodes with their representative spectra shown to the right corresponding to the numbered points in the maps. Scale bar = 20 μ m.

trations of Mn₃O₄ and Li₄Mn₅O₁₂ after full voltage range degradation.

Meng et al. similarly used Raman spectroscopy to observe the build-up of the ~ 650 cm⁻¹ degradation peak over 50 cycles in an LMO battery cathode.^[55] The work assigned this peak solely to the Mn₃O₄ species, however, as discussed above, it is not possible to explicitly distinguish between the contributions of Mn₃O₄ from Li₄Mn₅O₁₂ when mixed in LMO. Nevertheless, the study was successful in demonstrating the effectiveness of using Raman spectroscopy to link the ~ 650 cm⁻¹ peak increase to the progressing degradation. Though their findings were made in the context of a battery, the Raman maps presented in Figure 6 provide apparent evidence of this trend occurring in supercapacitors as well and is indicative of similar modes of failure.

Unfortunately, the battery investigation by Meng et al. only studied three point-spectra, which they considered representative and reproducible. It is however clear from our study (see the maps in Figure 6) that severe inhomogeneity in surface

activity and electrode material occurs in LMO-based cathodes, suggesting that studying localized phenomena may lead to misinterpretation. This is likely the reason that features like those found in the dominant hotspots, where the degradation peak becomes most prominent (as represented by spectra 6, 8 and 9), were not observed in the previously reported Raman investigation. This data therefore highlights that mapping allows for a much more complete picture of the surface activity and can enable earlier detection of the degradation species. Most importantly, it is essential to provide insights on the heterogeneity of the degradation across the electrode surface.

Interestingly, a noticeable improvement in the cycle life was observed when the voltage range was reduced from the full range of 0–2.3 V to either 0.01–2.3 V or 0.1–2.3 V in an effort to avoid stressing the cell at 0 V (Figure S12). This extended the cell lifetime to ~ 8300 and ~ 9000 cycles, respectively, before failure. Cycling over the range of 0.2–0.75 V showed a very significant improvement in cell lifetime to $\sim 92,500$ cycles, (Figure S13a) however these conditions only achieved a max-

imum capacitance of 130 F, 43% of the cell's rated capability (Figure S13b). Cycling the cell in only the high voltage range (HVR) region of 1.15–2.3 V yielded a 62% capacity retention (188 F) after 100,000 cycles as well as a significantly improved self-discharge (Figure S11). Thus, a clear trend of improved cyclability in higher voltage range regions was observed.

The Raman map of the HVR electrode showed a much milder and more uniform increase in the degradation species concentration, as opposed to the random clusters found in the FVR electrode (Figure 6). As the HVR cell never fully degraded, the results further link the observed lack of developing degradation hotspots with an improved cell performance (Figure S11). The spectra collected for this map (Figure 6, spectra 4–6) were more comparable to those given by Meng et al., in which the degradation signal located at $\sim 653\text{ cm}^{-1}$ (peak 6) is a prominent shoulder to the ~ 625 LMO peak (peak 5) as opposed to the dominant peak itself. As evidenced here, the simple presence of such a signal is not in fact in itself indicative of a failed/failing electrode. Instead, evidence of spectra like those of 8 and 9 should be used to indicate severe degradation due to detrimentally high concentrations of Mn_3O_4 and $\text{Li}_4\text{Mn}_5\text{O}_{12}$ in supercapacitors as well as battery systems.

As discussed above, a second known contributing degradation mechanism for LMO in batteries concerns the formation of tetragonal $\text{Li}_2\text{Mn}_2\text{O}_4$ on the surface of the electrode due to over-lithiation during periods of deep discharge (low voltages). As LiMn_2O_4 consists of equal amounts of cubic trivalent manganese and tetragonal tetravalent manganese, it has a theoretical average oxidation state of +3.5. Upon charging, the de-insertion of Li ions oxidizes LiMn_2O_4 to $\text{Li}_x\text{Mn}_2\text{O}_4$ ($0 \leq x \leq 1$) resulting in an oxidation state change towards +4.^[56] In the range of $0 \leq x \leq 1$, the crystal structure remains cubic, however, as the $\text{Li}_x\text{Mn}_2\text{O}_4$ spinel can accommodate up to $x=2$, over-insertion of Li ions during discharge is thought to form tetragonal $\text{Li}_2\text{Mn}_2\text{O}_4$ with an oxidation state of +3. An overall volume increase of 6.5% results^[57] as the cubic-to-tetragonal transformation is not entirely reversible.^[57–59] This can lead to microstrains and structural disorder that can reduce particle-to-particle contact at the cubic/tetragonal interface and may also cause a decreased electron conductivity and loss of capacity.

Lui et al. proposed a mechanism that aimed to explain the relationship between these two degradation processes and close the long-standing gap between Mn dissolution, structural evolution and their consequence.^[44] In this work, they put forward a 'vicious cycle' model in which charging induces the Mn^{3+} disproportionation reaction that forms soluble Mn species, and discharging promotes irreversible cubic-to-tetragonal phase transitions and crack propagation; together, these processes create a cycle of attack to diminish the capacity of LMO electrodes.

However, though tetragonal $\text{Li}_2\text{Mn}_2\text{O}_4$ has a distinct XRD pattern, no evidence of these signatures is apparent in the PXRD data presented in Figure 4(a) above, suggesting the bulk material in the commercial supercapacitor studied is still largely comprised of LiMn_2O_4 after 100,000 cycles. Yet, this apparent absence could be explained by its low percentage inclusion, primarily at particle interfaces, or random, microcrystalline

domains which lead to little long-range order. Notably, Mn_3O_4 was also not detected, although its presence was identified in the Raman maps. The diffraction pattern of the other degradation species, $\text{Li}_4\text{Mn}_5\text{O}_{12}$, is very similar to that of LiMn_2O_4 making its presence difficult to distinguish.^[54] Figure S14 compares diffractograms of Mn_3O_4 and $\text{Li}_4\text{Mn}_5\text{O}_{12}$ with that of the pseudocapacitor cathode after cycling.

However, Raman spectroscopy is surface sensitive and can detect low concentrations of $\text{Li}_2\text{Mn}_2\text{O}_4$, as it was shown to for Mn_3O_4 and $\text{Li}_4\text{Mn}_5\text{O}_{12}$, yet Raman mapping did not detect any signal of tetragonal $\text{Li}_2\text{Mn}_2\text{O}_4$ formation in any degraded electrode studied. This suggests that this species, which is integral to the degradation model for LMO batteries proposed by Liu et al., may not have in fact formed. This is further evidenced by the XPS analysis of the cathode material (Figure S15).

High-resolution XPS spectra of the $\text{Mn } 2p_{3/2}$ and $\text{Mn } 2p_{1/2}$ peaks are shown in Figure S16 and are centered around binding energies of 642.39 and 653.99 eV for the pristine and 642.99 and 655.28 eV for the degraded samples, respectively. While a quantitative analysis of mixed Mn oxides is very challenging due to significant multiplet splitting,^[60] a qualitative analysis of the Mn spectra using two equivalent asymmetric peaks to represent the overall envelope of Mn oxides shows a consistent and significant shift to higher binding energies from the pristine to cycled cathode (Figure S16). This is consistent with a major increase in Mn^{4+} species such as LiMn_2O_4 , or more likely $\text{Li}_4\text{Mn}_5\text{O}_{12}$ produced by the Hunter mechanism. The near total disappearance of Mn^{3+} species at the cathode surface supports the evidence from Raman spectroscopy that little tetragonal phase $\text{Li}_2\text{Mn}_2\text{O}_4$ was present.

As the electrodes are both sampled in their discharged state, the large increase in the +4 form is consistent with the understanding of the Hunter mechanism as the key mode of degradation. The battery literature commonly states that Jahn-Teller distortions occur in the $\text{Li}_x\text{Mn}_2\text{O}_4$ structure when $x > 1$, resulting in cubic-to-tetragonal phase transitions. However, when $x > 1$, the oxidation state of Mn in $\text{Li}_x\text{Mn}_2\text{O}_4$ moves below +3.5, which also results in the disproportionation of the Mn in the +3 state to a mix of +4 and +2 to balance the system [Eq. (2)]. As no detectable signal for tetragonal $\text{Li}_2\text{Mn}_2\text{O}_4$ (Mn valence state of +3) was found in any analysis of the cycled cathode, such significant growth in the proportion of the Mn^{4+} form as compared to Mn^{3+} after cycling indicates that in the pseudocapacitor the LMO is never sufficiently over-lithiated within the cycled voltage range to form meaningful amounts of tetragonal $\text{Li}_2\text{Mn}_2\text{O}_4$. Therefore, the primary mode of degradation in the LMO structure is attributed to the manganese disproportionation mechanism and its physical consequences, i.e., development of microstrains, particle fragmentation/isolation and loss of electrode conductivity, with negligible contributions from cubic-to-tetragonal phase transitions.

Conclusions

This work represents the first study to examine the aging and degradation of any supercapacitor from a full-cell perspective, by pairing in-situ, multi-length scale microscopic analysis with advanced spectroscopic analysis and complementary tear-down analysis for an exemplar commercial system. Importantly, we conclusively demonstrate that the reputation supercapacitors have for extended life cycle stability and reliability is not universally true. In fact, we show that some supercapacitor chemistries, even ones that have been utilized commercially, can degrade swiftly and prematurely.

The Li-ion pseudocapacitor system studied here consistently suffered from significant capacity loss (~96%) within the first 2000 charge/discharge cycles, despite it being rated for up to 100,000. Pre- and post-mortem X-ray CT characterization provided evidence of minimal active material loss (~5.5%), likely attributed to the dissolution of the Mn²⁺ via the Hunter mechanism. Yet, particle cracking and division was seen to be a major issue. Raman scattering analysis demonstrated that the localized accumulation of Mn₃O₄ and Li₄Mn₅O₁₂ is a fingerprint of the capacity collapse. It also emphasized the importance of utilizing mapping techniques in detecting signals of LMO material degradation, which can account for the inhomogeneity of the electrode surface, something which point spectra alone cannot do.

The clear trend of improved cyclability in reduced voltage ranges (avoiding low voltage) indicates that degradation is primarily associated with 'over-lithiation' during periods of deep discharge in this supercapacitor cell chemistry. Yet, there is no evidence of significant material dissolution or cubic-to-tetragonal phase changes, which are often associated with LMO in batteries. Instead, manganese disproportionation forming surface Mn²⁺ in the form of Mn₃O₄ (a species less conductive than LMO itself) is found to correlate with the onset of capacity fade and promotes the development of microstrains, particle fragmentation and electronic material isolation. Hence, this work proposes a deviation from the current understanding of LMO material degradation, which has thus far mainly been understood through the study of battery systems. By applying these techniques to battery LMO electrodes, future studies can help us understand if these processes are specific to supercapacitor LMO or apply to LMO applications more widely.

Thus, we have shown that understanding the modes of degradation in supercapacitors is vital for the future development of this key technology. If this is not widely achieved, supercapacitor success will lag behind that of other energy storage systems. Importantly, this understanding can't simply be achieved through an extension of the understanding developed via batteries, as here our work clearly shows that even similar materials will behave differently within the unique supercapacitor environment.

Experimental Section

Electrochemical cycling

Maxwell Technologies 2.3 V, 300 F pseudocapacitor cells (Maxwell Model Number: PCAP0300 P230 S07) have a projected lifetime of 100,000 constant current charge-discharge cycles at room temperature. The cells are rated up to 2.3 V and are stated to be able to withstand a maximum peak current of 53 A.^[25] The cells in this study were subjected to electrochemical cycling on an Arbin Instruments cell cycler, using MITS Pro 4.32 software, over the rated 100,000 constant current charge/discharge cycles from 0 to 2.3 V at a current of 5 A with a 30 second rest after charge and a 10 s rest after discharge. The term 'rest' in this case indicates no current being applied/drawn. The cell's operating temperature range is stated to be between -25 °C and 60 °C, so all tests were performed at ambient room temperature and no significant cell heating was observed. Hence, all testing conditions remained within the manufacturer specified limits. Cycling tests over the voltage ranges of 0.01–2.3 V, 0.1–2.3 V, 0.2–0.75 V and 1.15–2.3 V were also performed.

Electrode characterization

Raman mapping was performed using a Renishaw inVia confocal micro-Raman spectrometer, equipped with a 785 nm laser. The laser was focused to give a spot size of approx. 1.3 μm and the power at the sample was kept below 5.7 mW for an exposure time of 10 s. No transformation of the sample was observed under these irradiation conditions. The maps were made up of 676 points covering 50×50 μm with a step size of 2 μm. Occasional random spikes due to cosmic rays impacting the detector were removed using a custom method based on that proposed by Whitaker and Hayes.^[61] All peaks were fitted using a Lorentzian line shape.

X-ray diffraction (XRD) was undertaken using a Stoe STADI-P powder diffraction system with an X-ray radiation source of Mo K_{α1}. Electrode material was scraped off the aluminum current collector using a razor blade and the powder was mounted onto the sample holder. Diffraction patterns were acquired in a 2θ range of 2.000° to 40.115° with a step size of 0.495° at a rate of 10.0 s/step. The SmartLab II x64 v4 1.0.182 software was used to assess spectral peaks and values were compared with spectra recorded in the program database.

Scanning electron microscopy (SEM) was performed using a Zeiss UltraPlus analytical FESEM device equipped with Oxford Instruments INCAx.act EDXA system (10 mm 2 Silicon Drift Detector, ATW 129 eV). The Zeiss SmartSEM V05.06 operating software was used to process the data. SEM images of the cathode were taken at 15,000x magnification at an accelerating voltage of 10 kV.

Quantitative gas analysis was performed on the electrolyte solvent using a QGA mass spectrometer (Hiden analytical) in a mass to charge ratio range of 0–60.

X-ray photoelectron spectroscopy (XPS) was performed on the electrolyte salt as well as both electrodes by scraping material off of the aluminum current collectors. A thermoscientific K-alpha XPS machine with a monochromatic Al K_α X-ray source of 1,486.68 eV energy and spot size of 400 μm was used. The data was processed using the CasaXPS Version 2.3.19 software.

X-ray computed tomography

Three different X-ray computed tomography (CT) systems were used to compare pre- and post-cycled electrodes. Scans of the full

cell in its initial and final states were taken on a Nikon XTH 225 kV. The pristine cell was scanned using a beam energy of 135 kV, beam current of 65 μ A, pixel size of 25 μ m, exposure of 1 second with 2512 projections. After cycling, the degraded cell was scanned using a beam energy of 135 kV, beam current of 60 μ A, pixel size of 25 μ m, exposure of 1 second and 2470 projections.

Ex-situ X-ray nano-CT was performed on the laser-milled tab electrode samples (see below) using a lab-based nano-CT instrument (ZEISS Xradia 810, 5.4 keV Ultra, Carl Zeiss Inc.) for the highest resolution scans, with voxel resolution in the range of 16–128 nm with a field of view of ca. 15–65 μ m. The rotating Cr anode source was set to an accelerating voltage of 35 kV. Large field of view mode with a pixel binning of 1 was used for the pristine sample resulting in a pixel size of ca. 126.3 nm and a binning of 2 was used for the degraded sample resulting in a pixel size of ca. 63.1 nm. The sample was rotated through 180° with radiographs collected at discrete angular intervals amounting to 1601 projections. The projection data from each tomogram was run through proprietary reconstruction software (XMReconstructor, Carl Zeiss Inc.) using a parallel beam reconstruction algorithm. Sequential tomography sequences using absorption contrast and Zernike phase contrast were collected. Contributions from 25% of the phase mode and 75% of the absorption mode were stitched together in the Dual Scan Contrast Visualizer (DSCoVer) software. The obtained images were processed using the Avizo 3D visualization software package (Avizo, version 2020.2 FEIO, VSG).

X-ray sample tab preparation

X-ray CT samples were prepared using a laser micro-machining instrument (A Series, Oxford Lasers Ltd.) containing a 532 nm laser with a spot size of ca. 40 μ m following the methods outlined by C. Tan et al.^[62] The electrodes were cut into a tab consisting of 2 rectangular sections with the smaller section measuring ca. 0.2 mm × 0.08 mm and the larger section measuring ca. 2 mm × 4 mm.

Avizo image processing

Image processing was performed using the Avizo 3D visualization software package (Avizo, version 2020.2 FEIO, VSG) and segmentation was carried out via a simple thresholding algorithm. The initial image was cropped so that segmentation analysis focused on the bulk of the material and eliminated differences in attenuation contrast that arose from sample edges that had been exposed to the laser. The final transformed volume of the pristine sample contained 250 × 203 × 410 voxels at a size of 126.3 × 126.3 × 126.3 nm per voxel and the degraded sample contained 567 × 721 × 473 voxels at a size of 63.1 × 63.1 × 63.1 nm per voxel.

Non-local means and unsharp masking filters were applied to the dataset to reduce noise and more clearly define the particle edges. Segmentation was performed three times and averaged between conservative, moderate and generous threshold methods to account for the subjectivity in image processing. Both the pristine and degraded sample datasets were processed similarly to make results comparable.

Small features less than 4 voxels wide were removed and the “Separate Objects” module was applied to detect and subtract out surfaces that separate agglomerate particles. The “Opening” module was used to reduce unnecessary artifacts and excess noise by removing small objects and smoothing object boundaries. Particles that were only partially captured within the volume were removed using the “Border Kill” module and finally, “Label Analysis”

was applied to collect statistical data of each particle in the sample. Tortuosity was calculated using the MatLab plugin, TauFactor.^[63]

Author Contributions

Conceptualization, K.M. and T.S.M.; Methodology, K.M. and T.S.M.; Software K.M. and H.J.L.; Validation, T.S.M.; Formal Analysis, K.M. and H.J.L.; Investigation, K.M. and H.J.L.; Resources, C.A.H., P.R.S. and T.S.M.; Writing – Original Draft, K.M. and H.J.L.; Writing – Review & Editing, T.S.M., C.A.H. and P.R.S.; Visualization, K.M., H.J.L. and T.S.M.; Supervision, T.S.M., C.A.H. and P.R.S.; Project Administration, K.M.; Funding Acquisition, T.S.M.

Acknowledgements

The present research has been supported by the Faraday Institution (EP/S003053/1) degradation project (FIRG001) and LiSTAR project (FIRG014). PRS acknowledges The Royal Academy of Engineering (CiET1718/59). KM acknowledges support from the UCL H. Walter Stern Scholarship.

Conflict of Interests

The authors declare no conflict of interest.

Data Availability Statement

The data that support the findings of this study are available from the corresponding author upon reasonable request.

Keywords: lithium-ion capacitor • lithium manganese oxide • LMO • Raman spectroscopy • X-ray computed tomography

- [1] D. P. Dubal, O. Ayyad, V. Ruiz, P. Gómez-Romero, *Chem. Soc. Rev.* **2015**, *44*, 1777–1790.
- [2] Z. Zhao, K. Xia, Y. Hou, Q. Zhang, Z. Ye, J. Lu, *Chem. Soc. Rev.* **2021**, *50*, 12702–12743.
- [3] H. Yoo, S. K. Sul, Y. Park, J. Jeong, *IEEE Trans. Ind. Appl.* **2008**, *44*, 108–114.
- [4] I. Must, F. Kaasik, I. Pöldsalu, L. Mihkels, U. Johanson, A. Punning, A. Aabloo, *Adv. Eng. Mater.* **2015**, *17*, 84–94.
- [5] G. Oriti, N. Anglani, A. L. Julian, *IEEE Trans. Ind. Appl.* **2019**, *55*, 5099–5108.
- [6] C. Meng, O. Z. Gall, P. P. Irazoqui, *Biomed. Microdevices* **2013**, *15*, 973–983.
- [7] B. K. Kim, S. Sy, A. Yu, J. Zhang, *Handb. Clean Energy Syst.* **2015**, 1–25.
- [8] A. J. Paleo, P. Staiti, A. M. Rocha, G. Squadrito, F. Lufrano, *J. Power Sources* **2019**, *434*, 226735.
- [9] W. Raza, F. Ali, N. Raza, Y. Luo, K. H. Kim, J. Yang, S. Kumar, A. Mehmood, E. E. Kwon, *Nano Energy* **2018**, *52*, 441–473.
- [10] Eaton, TVA Supercapacitors Automotive grade cylindrical cells, www.eaton.com/electronics, (accessed 16 January 2023).
- [11] Maxwell Technologies, Advanced Small Cell with Snap-In Terminals, http://www.mouser.co.uk/datasheet/2/257/3003111-EN.1_3V_100F_Datasheet-1879326.pdf, (accessed 10 July 2022).
- [12] A. Adib, R. Dhaouadi, *2017 7th Int. Conf. Model. Simulation, Appl. Optim. ICMSAO 2017*, 10.1109/ICMSAO.2017.7934897.

- [13] F. Naseri, E. Farjah, T. Ghanbari, *IEEE Trans. Veh. Technol.* **2017**, *66*, 3724–3738.
- [14] E. Frackowiak, F. Béguin, *Carbon* **2001**, *39*, 937–950.
- [15] P. Simon, Y. Gogotsi, *Nat. Mater.* **2008**, *7*, 845–854.
- [16] F. Rafik, H. Gualous, R. Gallay, A. Crasaz, A. Berthon, *J. Power Sources* **2007**, *165*, 928–934.
- [17] M. Ayadi, O. Briat, R. Lallemand, A. Eddahech, R. German, G. Coquery, J. M. Vinassa, in *Microelectronics Reliability*, Elsevier Ltd, **2014**, vol. 54, pp. 1944–1948.
- [18] O. Bohlen, J. Kowal, D. U. Sauer, *J. Power Sources* **2007**, *172*, 468–475.
- [19] M. Ebner, F. Geldmacher, F. Marone, M. Stampanoni, V. Wood, *Adv. Energy Mater.* **2013**, *3*, 845–850.
- [20] J. Gelb, D. P. Finegan, D. J. L. Brett, P. R. Shearing, *J. Power Sources* **2017**, *357*, 77–86.
- [21] D. P. Finegan, M. Scheel, J. B. Robinson, B. Tjaden, I. Hunt, T. J. Mason, J. Millichamp, M. Di Michiel, G. J. Offer, G. Hinds, D. J. L. Brett, P. R. Shearing, *Nat. Commun.* **2015**, *6*, 1–10.
- [22] D. S. Eastwood, V. Yufit, J. Gelb, A. Gu, R. S. Bradley, S. J. Harris, D. J. L. Brett, N. P. Brandon, P. D. Lee, P. J. Withers, P. R. Shearing, *Adv. Energy Mater.* **2014**, *4*, 1300506.
- [23] P. Schlee, S. Herou, R. Jervis, P. R. Shearing, D. J. L. Brett, D. Baker, O. Hosseini, P. Tomani, M. M. Murshed, Y. Li, M. J. Mostazo-López, D. Cazorla-Amorós, A. B. Jorge Sobrido, M. M. Titirici, *Chem. Sci.* **2019**, *10*, 2980–2988.
- [24] D. I. Abouelamaiem, G. He, I. Parkin, T. P. Neville, A. B. Jorge, S. Ji, R. Wang, M. M. Titirici, P. R. Shearing, D. J. L. Brett, *Sustain. Energy Fuels* **2018**, *2*, 772–785.
- [25] Maxwell Technologies, Datasheet: 2.3V 300F PSEUDOCAPACITOR CELL, http://www.mouser.co.uk/datasheet/2/257/2_3_300F_ds_3001971_datasheet-1568351.pdf, (accessed 16 January 2023).
- [26] G. A. dos Santos Junior, V. D. S. Fortunato, G. G. Silva, P. F. R. Ortega, R. L. Lavall, *Electrochim. Acta* **2019**, *325*, 134900.
- [27] Electrochemical Supercapacitors: Scientific Fundamentals and Technological ... – B. E. Conway-Google Books, <https://books.google.co.uk/books?hl=en&lr=&id=zCblBwAAQBAJ&oi=fnd&pg=PA1&dq=B. E.+Conway,+Electrochemical+supercapacitors:+scientific+fundamentals+and+technological+applications,+Springer+Science+%26+Business+Media2013&ots=bajCeqZwtA&sig=W49O0brmFDKmgUDUw-LJZf9mS84#v=onepage&q&f=false>, (accessed 26 April 2021).
- [28] M. Marcinek, J. Syzdek, M. Marczewski, M. Piszzcz, L. Niedzicki, M. Kalita, A. Plewa-Marczewska, A. Bitner, P. Wieczorek, T. Trzeciak, M. Kasprzyk, P. Łęzak, Z. Zukowska, A. Zalewska, W. Wieczorek, *Solid State Ionics* **2015**, *276*, 107–126.
- [29] X. Y. Yao, M. G. Pecht, *IEEE Access* **2019**, *7*, 24082–24095.
- [30] A. Gabryelczyk, S. Ivanov, A. Bund, G. Lota, *J. Energy Storage* **2021**, *43*, 103226.
- [31] A. Jnawali, A. N. P. Radhakrishnan, M. D. R. Kok, F. Iacoviello, D. J. L. Brett, P. R. Shearing, *J. Power Sources* **2022**, *527*, 231150.
- [32] M. D. R. Kok, J. B. Robinson, J. S. Weaving, A. Jnawali, M. Pham, F. Iacoviello, D. J. L. Brett, P. R. Shearing, *Sustain. Energy Fuels* **2019**, *3*, 2972–2976.
- [33] Y. Li, C. Wei, Y. Sheng, F. Jiao, K. Wu, *Ind. Eng. Chem. Res.* **2020**, *59*, 30.
- [34] C. Chen, Y. Wei, Z. Zhao, Y. Zou, D. Luo, *Electrochim. Acta* **2019**, *305*, 65–71.
- [35] F. Tuinstr, J. L. Koenig, *J. Chem. Phys.* **2003**, *53*, 1126.
- [36] A. C. Ferrari, D. M. Basko, *Nat. Nanotechnol.* **2013**, *8*, 235–246.
- [37] F. Zhang, T. Geng, F. Peng, D. Zhao, N. Zhang, H. Zhang, S. Li, *ChemElectroChem* **2019**, *6*, 731–740.
- [38] V. Paulraj, B. Swami, K. Kamala Bharathi, *Appl. Phys. Lett.* **2019**, *115*, 093901.
- [39] Y. Xia, Y. Zhou, M. Yoshio, *J. Electrochem. Soc.* **1997**, *144*, 2593–2600.
- [40] T. Inoue, M. Sano, *J. Electrochem. Soc.* **1998**, *145*, 3704–3707.
- [41] C. F. Holder, R. E. Schaak, *ACS Nano* **2019**, *13*, 7359–7365.
- [42] H. L. Zhu, Z. Y. Chen, S. Ji, V. Linkov, *Solid State Ionics* **2008**, *179*, 1788–1793.
- [43] J. C. Hunter, *J. Solid State Chem.* **1981**, *39*, 142–147.
- [44] T. Liu, A. Dai, J. Lu, Y. Yuan, Y. Xiao, L. Yu, M. Li, J. Gim, L. Ma, J. Liu, C. Zhan, L. Li, J. Zheng, Y. Ren, T. Wu, R. Shahbazian-Yassar, J. Wen, F. Pan, K. Amine, *Nat. Commun.* **2019**, *10*, 1–11.
- [45] D. Tang, Y. Sun, Z. Yang, L. Ben, L. Gu, X. Huang, *Chem. Mater.* **2014**, *26*, 3535–3543.
- [46] H. Konieczna, D. Lundberg, I. Persson, *Polyhedron* **2021**, *195*, 114961.
- [47] H. Huang, C. A. Vincent, P. G. Bruce, *J. Electrochem. Soc.* **1999**, *146*, 3649–3654.
- [48] M. M. Thackeray, Y. Shao-Horn, A. J. Kahaian, K. D. Kepler, E. Skinner, J. T. Vaughan, S. A. Hackney, *Electrochim. Solid-State Lett.* **1998**, *1*, 7–9.
- [49] J. M. Tarascon, W. R. McKinnon, F. Coowar, T. N. Bowmer, G. Amatucci, D. Guyomard, *J. Electrochim. Soc.* **1994**, *141*, 1421–1431.
- [50] C. Zhan, T. Wu, J. Lu, K. Amine, *Energy Environ. Sci.* **2018**, *11*, 243–257.
- [51] Y. Xia, Y. Zhou, M. Yoshio, *J. Electrochim. Soc.* **1997**, *144*, 2593–2600.
- [52] C. M. Julien, M. A. Camacho-Lopez, *Mater. Sci. Eng. B* **2004**, *108*, 179–186.
- [53] C. M. Julien, M. Massot, C. Poinsignon, *Spectrochim. Acta Part A* **2004**, *60*, 689–700.
- [54] C. M. Julien, M. Massot, *Mater. Sci. Eng. B* **2003**, *100*, 69–78.
- [55] X. Meng, Z. Bi, P. Lou, G. Shang, *Langmuir* **2022**, *38*, 3887–3895.
- [56] F. Luo, C. Wei, C. Zhang, H. Gao, J. Niu, W. Ma, Z. Peng, Y. Bai, Z. Zhang, *J. Energy Chem.* **2020**, *44*, 138–146.
- [57] B. Slautin, D. Alikin, D. Rosato, D. Pelegov, V. Shur, A. Khoklin, *Batteries* **2018**, *4*, 21.
- [58] T. Erichsen, B. Pfeiffer, V. Roddatis, C. A. Volkert, *ACS Appl. Energ. Mater.* **2020**, *3*, 5405–5414.
- [59] X. C. Tang, B. Y. Huang, Y. H. He, *Trans. Nonferrous Met. Soc. China* **2006**, *16*, 438–444.
- [60] M. C. Biesinger, B. P. Payne, A. P. Grosvenor, L. W. M. Lau, A. R. Gerson, R. S. C. Smart, *Appl. Surf. Sci.* **2011**, *257*, 2717–2730.
- [61] D. A. Whitaker, K. Hayes, *Chemom. Intell. Lab. Syst.* **2018**, *179*, 82–84.
- [62] C. Tan, S. Daemi, T. Heenan, F. Iacoviello, A. S. Leach, L. Rasha, R. Jervis, D. J. L. Brett, P. R. Shearing, *J. Electrochim. Soc.* **2020**, *167*, 060512.
- [63] S. J. Cooper, A. Bertei, P. R. Shearing, J. A. Kilner, N. P. Brandon, *SoftwareX* **2016**, *5*, 203–210.

Manuscript received: May 19, 2023

Revised manuscript received: June 7, 2023

Accepted manuscript online: June 9, 2023

Version of record online: June 29, 2023